Advanced interferometric techniques for high resolution bathymetry

Gerard Llort Pujol, Christophe Sintes, Thierry Chonavel, Archie T. Morrison, Sylvie Daniel

Advanced interferometric techniques for high-resolution bathymetry

Gerard Llort-Pujol, *Member*, IEEE, Christophe Sintes, *Senior Member, IEEE*, Thierry Chonavel, *Member, IEEE*, Archie T. Morrison III, *Senior Member, IEEE*, and Sylvie Daniel, *Member, IEEE*

***Abstract*— Current high-resolution side scan and multibeam sonars produce very large data sets. However, conventional interferometry-based bathymetry algorithms underestimate the potential information of such soundings, generally because they use small baselines to avoid phase ambiguity. Moreover, these algorithms limit the triangulation capabilities of multibeam echosounders to the detection of one sample per beam, i.e., the zero-phase instant. In this paper we argue that the correlation between signals plays a very important role in the exploration of a remotely observed scene. In the case of multibeam sonars, capabilities can be improved by using the interferometric signal as a continuous quantity. This allows consideration of many more useful soundings per beam and enriches understanding of the environment. To this end, continuous interferometry detection is compared here, from a statistical perspective, first with conventional interferometry-based algorithms and then with high-resolution methods, such as the Multiple Signal Classification (MUSIC) algorithm. We demonstrate that a well-designed interferometry algorithm based on a coherence error model and an optimal array configuration permits a reduction in the number of beam formings (and therefore the computational cost) and an improvement in target detection (such as ship mooring cables or masts). A possible interferometry processing algorithm based on the complex correlation between received signals is tested on both sidescan sonars and multibeam echosounders and shows promising results for detection of small in-water targets.**

***Index Terms*— Sonar detection, interferometry, performance analysis, beam steering, object detection.**

I. INTRODUCTION

A. Context

Seafloor exploration is a major objective in many fields, ranging from military applications to civilian industries. This paper focuses on cartographic applications that need accurate bathymetric measurements with full-swath coverage. Typical applications are seafloor mapping for geosciences and hydrography, shipwreck inspections, and pipeline surveys.

Current acoustic methods of seafloor cartography are mainly dominated by multibeam echosounders (MBES), although phase-differencing bathymetric sidescan sonars are becoming real challengers. MBES systems can, after transmission of a single signal, perform a large number of soundings on a wide strip of terrain perpendicular to the ship track. This paper is intended to move the performance of multibeam systems a step forward by improving their spatial resolution while maintaining current accuracy levels. We have concentrated in this paper work carried out in recent years on the analytical formalism of interferometry performance, comparisons with other existing methods, and different approaches to implementation in multibeam systems.

Manuscript received -, 2011.

Gerard Llort-Pujol, Christophe Sintes, and Thierry Chonavel are with Telecom Bretagne, CNRS Lab-STICC/CID, Technopôle Brest-Iroise, CS 83818 - 29238 Brest Cedex 3, France. (Corresponding author e-mail: gerard.llort@telecom-bretagne.eu)
Archie T. Morrison III is with Woods Hole Group, Inc, 81 Technology Park Drive, East Falmouth, MA 02536, USA.
Sylvie Daniel is with the Department of geomatics sciences, Laval University, Quebec, GC G1V 0A6, Canada.

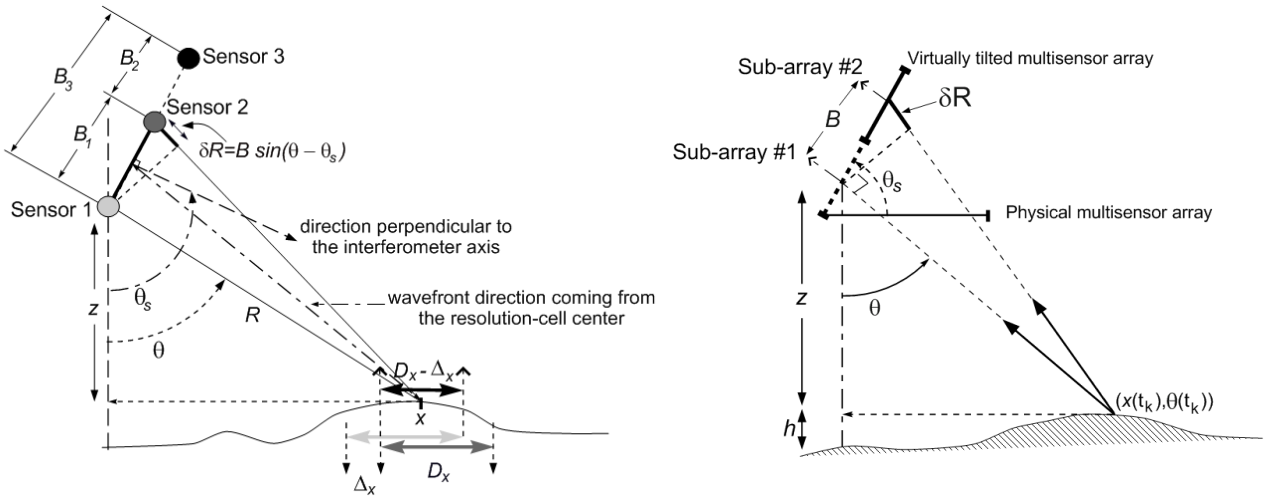

Fig. 1. Three-sensor-based sidescan (left panel) and multibeam (right panel) interferometry geometry, defining the baselines B_i, propagation-path delay δR between sensors 1 and 2, common arrival angle θ, tilt angle θ_s, and altitude z. Definition of the parameters used to evaluate the range-shift decorrelation including the resolution-cell size D_x and the footprint shift Δ_x.

B. What is interferometric bathymetry?

With the increase in processing and storage capacity of remote sensing systems, current multibeam bottom detectors should not be content with only a high-resolution description of the sea bottom. Other targets in the water column, such as ship masts or mooring chains, can actually be detected by current multibeam technology as previously by sidescan and synthetic aperture sonars. Bathymetry is derived from measurements of ocean depth made by depth sounding. Two approaches can be considered to estimate water depths for a given beam forming: either the estimation of the time of arrival (TOA) of backscattered signals for a predefined tilt angle or the estimation of the direction of arrival (DOA) for a given instant of time. Multibeam echosounders are used to determine the two-way propagation distance of a single emitted pulse by applying target detection techniques such as interferometry (Denbigh, 1989), subspace-based methods (Krim, 1996), or active contour detection (Yang, 1997). We have been specially looking into the interferometry method because of its simplicity and its speed. These characteristics are demonstrated throughout this paper.

The interferometry method is a relevant solution provided that the illuminated area is not too large and it is well adapted for oblique and grazing angles (Masnadi-Shirazi, 1992; Jin, 1996). This technique provides accurate bathymetric information from the phase shift $\Delta\Phi$. This shift arises when the backscattered wave front reaches two close receivers at different instants (see Fig. 1). Thus, $\Delta\Phi$ is geometrically related to the path-length difference δR, giving

$$\Delta\Phi = \frac{2\pi}{\lambda}\delta R = \frac{2\pi}{\lambda} B \sin\left(\theta_s - \theta\right) \tag{1}$$

This means that the true direction of the noiseless wave front, denoted here θ, can be determined from the phase shift $\Delta\Phi$. In other words, at each instant of time, we can determine the DOA of the signal by converting each measurement $\Delta\Phi$ into an angular measurement θ, and by triangulation, the coordinate position of the in-water target. The other parameters in (1), such as the tilt angle θ_s, the spacing B between the two sensors, commonly called the *baseline*, or the acoustic wavelength λ, depend on the sonar configuration and are supposed to be well known. Note that (1) is true for an isotropic and non-dispersive medium assuming a stationary noise process and far field propagation.

As the direction of the wave front is directly related to the phase shift $\Delta\Phi$, the goal now is to find a way to measure this shift. A usual approach is to measure the difference $\Delta\varphi$ between the phases of the two signals S_1 and S_2 of each receiver related to a path

delay between sensors.

$$\Delta\hat{\varphi} = \arg\ \ s_1 s_2^* \tag{2}$$

The operator arg{x} gives the phase of a complex value x, and S_2* stands for the complex conjugate of signal S received by the second sensor. The parameter $\Delta\hat{\varphi}$ corresponds to an estimation of the phase difference Δφ. An estimator is used in a statistical model to infer the value of an unknown parameter based on observed data. Thus, an estimator of x is denoted here by the symbol $\hat{x}$.

The problem of the argument operator arg{x} is that it delivers values within a 2π-length interval. Indeed, the true phase shift may take values greater than 2π, but the argument operator truncates them. The result, displayed in Fig. 5 (lower panel), is a set of phase jumps when a phase measurement exceeds 2π. In order to interpret this figure, let us assume a flat sea floor whose representation is a horizontal line with a constant depth. If we convert this Cartesian coordinate system (depth, across-track distance) to a polar system (distance from the sonar to the sea floor or range, DOA), the result is a bell-shaped curve with a peak corresponding to the range at the nadir. Finally, if the DOA is converted to phase measurement ΔΦ using (1), the resulting form is also a bell. Each time we form a beam, a small part of the sea floor is insonified. In other words, the beamforming provides a piece of this bell corresponding to a curve. When this curve is estimated through (2), the resulting phase values are truncated between –π and π radians (or -180º and 180º), leading to the saw-tooth shape of samples between sample #600 and #800 depicted in Fig. 5 (lower panel). The rest of samples in this panel correspond to noise recorded by the hydrophones before and after the arrival of the wave front. A way to distinguish useful samples from noisy ones is discussed in Section IV.

In order to compensate for this truncation and obtain a whole curve without discontinuities, a phase-rotation counter m is necessary to link the phase difference Δφ with the phase shift ΔΦ:

$$\Delta\varphi + 2\pi m = \Delta\Phi \tag{3}$$

The counter m takes here integer values. The final interferometry equation, linking the estimator $\Delta\hat{\varphi}$ of the phase difference and the estimator $\hat{\theta}$ of the direction of arrival, is written as:

$$\Delta\hat{\varphi} = \frac{2\pi}{\lambda} B \sin\ \ \theta_s - \hat{\theta}\ \ + 2\pi m \tag{4}$$

Consequently, the estimated phase difference is ambiguous because the value of the rotational counter m is unknown.

Two important terms appear in (4): an absolute phase shift, corresponding to the sine term, and the 2πm rotations. In order to retrieve the absolute shift, which leads to the target DOA estimation, it is necessary to measure the interferometric phase Δφ, and then to determine the rotation counter m. The phase ambiguity can be removed by either an edge-detection algorithm (Tribolet, 1977) (i.e. detecting phase jumps around π, and adding 2π to the phase difference) or an *ad hoc* method (Shensa, 1978; Sintes, 2010) locally estimating the m counter of each ambiguous phase sample. An interferometric phase ambiguity removal step is crucial to estimation of the target elevation angle θ and depth z.

So far, the description of the interferometry principle can be applied to sonar systems such as sidescan sonar, for which a single narrow sound beam is transmitted and received. As a result, the tilt angle θ_s of the receiver array is physically fixed at some given angle by the sonar supplier. Conversely, a MBES transmits and receives a fan of beams with small individual widths across the ship axis, and the tilt angle θ_s varies according to the desired beam direction. As a result, the physical detection geometry changes in such as way that the estimator of the phase difference can be written as

$$\Delta\hat{\varphi} = \frac{2\pi}{\lambda} B\left[\sin(\theta_s) - \sin(\hat{\theta})\right] + 2\pi m \tag{5}$$

The existence of two sine terms in (5) compared with the unique term in (1) is due to the beam forming geometry in reception.

As highlighted, what bathymetry seeks is to determine the coordinates of the measurement point, that is, time of arrival and direction of arrival of backscattered signals. To this end, most interferometry-based MBES bottom detectors seek to estimate the zero-phase instant (ZPI). Assuming farfield propagation conditions, when the backscattered signal reaches the two receivers perpendicularly to the interferometer line, i.e. $\theta=\theta_s$, the sine term (1) is null, resulting in a zero phase difference. This way, the coordinates of a point in the space are estimated as follows: the TOA of backscattered signals is defined by the ZPI, and the DOA is given by the beam pointing angle θ_s. The phase ramp (as a function of time) is usually fitted with a polynomial using a least squares fit whose intersection with the zero-phase axis provides the instant corresponding to the sounding (Lurton, 2003). This procedure delivers one sounding per beam. Therefore, the number of soundings contributing to the bathymetry depends on the number of formed beams.

Another approach for high-resolution bathymetry consists of converting all useful samples $\Delta\hat{\varphi}$ of a phase difference into DOA measurements $\hat{\theta}$ based on (6). This is commonly done in sidescan sonar systems (Kraeutner, 1999).

$$\hat{\theta} = \theta_s - \sin^{-1}\left(\frac{\Delta\hat{\varphi} + 2\pi m}{2\pi B / \lambda}\right) \tag{6}$$

Equation (6) yields a dense series of angular measurements as a function of time: indeed, the data density may be as high as given by the sampling frequency of the time signals. For instance, the beam forming that delivers the phase difference depicted in Fig. 5 would produce about 200 angular measurements.

In conclusion, two approaches can be considered:

- Estimation of the target range R (i.e. TOA) for a predefined angle θ (equal to the beam pointing angle θ_s), based on a polynomial fit of the phase ramp using N phase samples.
- Estimation of the DOA θ for a given instant $t=t_k$ based on (6) where $\Delta\varphi(t_k)$ could be the result of an N sample filtering process used to reduce the interferometric phase variance.

Now, let us quantify the levels of accuracy for these two approaches.

C. *Why interferometric bathymetry?*

To demonstrate why interferometry should be of interest, we will briefly examine the quality of soundings. Basically, a depth sounding z can simply be evaluated through trigonometry as

$$z = R\cos\theta \tag{7}$$

For the sake of simplicity, we present here a relative measurement error instead of a classical calculation based on variance estimators which would the right way to quantity statistical performances of an estimator. Thus, the relative depth measurement error $\delta z/z$ can be expressed as a function of the angular and range measurement errors as (Lurton, 2003):

$$\delta \ln z = \frac{\delta z}{z} = \frac{\delta R}{R} + \tan\theta\,\delta\theta \tag{8}$$

The term δz can be assimilated to $\sqrt{\mathrm{E}\left[\hat{z}^2\right]}$ where $\hat{z}$ represents an estimation of z. The same could be done for $\delta\theta$, $\delta\Delta\varphi$, and δt.

Equation (8) is composed of two terms: the first term, depending on δR, represents the part of the error corresponding to the TOA estimation. The second term is linked to the DOA measurement error. On one hand, if phase detection is based on (6), only the second term is considered because R is constant. Thus, the depth measurement error δz can be written as a function of the interferometric error $\delta\Delta\varphi$ based on (4), resulting in (Sintes, 2010):

$$\frac{\delta z}{z} = \frac{\lambda}{2\pi B \cos(\theta_s - \theta)} \tan\theta \ \delta\Delta\varphi \tag{9}$$

See then that the depth measurement error depends on sonar parameters such as the distance B between the two receivers or the acoustic wavelength λ.

On the other hand, the error in interferometry measurements based on ZPI detection only concerns the first term in (8) because θ is a constant value equal to θ_s, and therefore $\delta\theta$ is equal to zero. As a result,

$$\frac{\delta z}{z} = \frac{\delta R}{R} = \frac{\delta t}{t} \tag{10}$$

The simplest ZPI detection takes advantage of the time evolution shape of the interferometric phase and consists in a linear regression (LR) of the (assumed linear) phase ramp around the ZPI (Lurton, 2003). This approach, called here LR ZPI, can be improved by weighting the calculations with the amplitude of the cross product $s_1 s_2^*$, denoted here WLR ZPI (for weighted linear regression zero-phase instant). With this linear approximation of the interferometric phase difference, the depth measurement error δz becomes proportional to the interferometric phase error $\delta\Delta\varphi$. In other words, a time error can be converted into an interferometric phase error:

$$\Delta\varphi = at + b \Rightarrow \delta\Delta\varphi = a\delta t \tag{11}$$

The next step is to analyze the performances of these techniques. Thus, in order to quantify the depth estimation error based on a known ground truth, a Monte Carlo simulation was performed based on the parameters of a 300-kHz MBES composed of an array with 80 sensors at half wavelength spacing and a pulse length of 150 µs. The baseline of the interferometer was of 13λ. The seafloor was 23 meters deep and the beam pointing angle θ_s was preset at 50°. Under these conditions, a phase ramp composed of 41 time samples was simulated for a π radian dynamic range and with the true ZPI exactly in the center of the ramp.

Fig. 2 shows how the errors associated with the different estimators involved in this simulation have been computed: in the absence of noise, the linear regression leads to the solid curve without errors, whereas in the presence of noise, the linear regression is biased resulting in the dashed curve. For this figure, we assume that the phase ramp is a straight line near the ZPI for the sake of simplicity. Thus, two estimation errors can be considered: the error between the true ZPI and the estimated ZPI, and the estimation error between the true zero phase (solid curve) and non-zero phase (dashed curve) at the true ZPI. These estimation errors are called ZPI error and Phi error, respectively. As the ZPI error is given in the time domain (difference between two instants of time), and the Phi error is in the phase domain, the former must be converted into the phase domain in order to be compared with the Phi error.

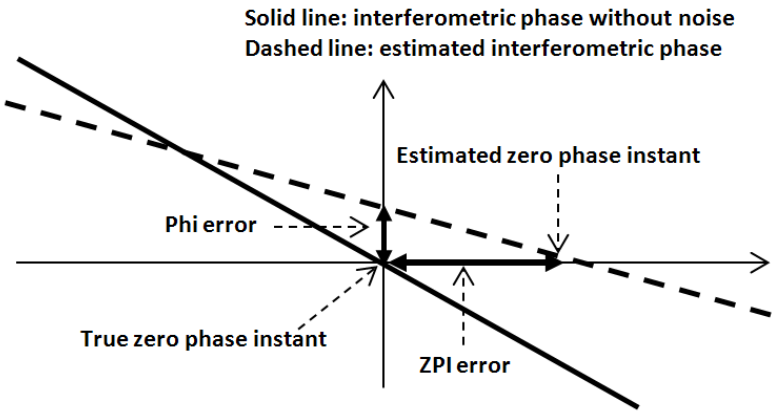

Fig. 2. Sketch showing two ways to compute the misdetection of the ZPI: (1) the Phi error represents the difference between noisy phase difference and true phase difference at true ZPI; (2) the ZPI error represents the difference between the true and the estimated instants of zero phase.

Finally, a stationary maximum likelihood estimator (SMLE) and a nonstationary maximum likelihood estimator (NSMLE) were also performed on these simulated data in order to enrich the estimation error comparison. The interest in such estimators lies in the fact that estimators based on a maximum likelihood criterion are known to produce estimates with the lowest possible variance (reaching the Cramer Rao bound) (Kendall, 1961). In our case, the SML estimator of N complex samples is given by (14) in (Masnadi-Shirazi, 1992):

$$\Delta\hat{\varphi} = \tan^{-1}\left\{\frac{\sum_{k=1}^{N} W^2(t_k)\,\mathrm{Im}\;\; S_1(t_k)S_2^*(t_k)}{\sum_{k=1}^{N} W^2(t_k)\,\mathrm{Re}\;\; S_1(t_k)S_2^*(t_k)}\right\} \tag{12}$$

$S_1(t_k)$ represents here the signal received by the first sensor at instant t_k, Re{x} and Im{x} are the real and imaginary parts of a complex value x, and W is a window function. Stationary estimators are widely implemented because they assume that the statistical characteristics of a given process (in our case, the mean, variance, and correlation of the received signal) do not change over time. Put another way, if one were to observe a stationary random process at some time t_1, its statistical characteristics would be the same as the one observed at some other time t_2. This is roughly the definition of a stationary process and an example is the noise received by sensors. However, the signal backscattered by an in-water target may not be stationary. Hence, (Llort-Pujol, 2012b) discusses the advantages of a nonstationary estimator and proves that coefficients a and b of the linear regression in (11) can be estimated as follows:

$$\begin{aligned}\hat{a} &= 2\pi \arg\;\max\left|FT(S_1S_2^*(t_k))\right| \\ \hat{b} &= \arg\sum_k S_1(t_k)S_2^*(t_k)e^{-j\hat{a}t_k}\end{aligned} \tag{13}$$

The argument operator arg of the first equation in (13) gives the maximum value of the Fourier transform FT of the product S_1S_2* at the instant t_k, while the same operator in the second equation gives the phase of the summation.

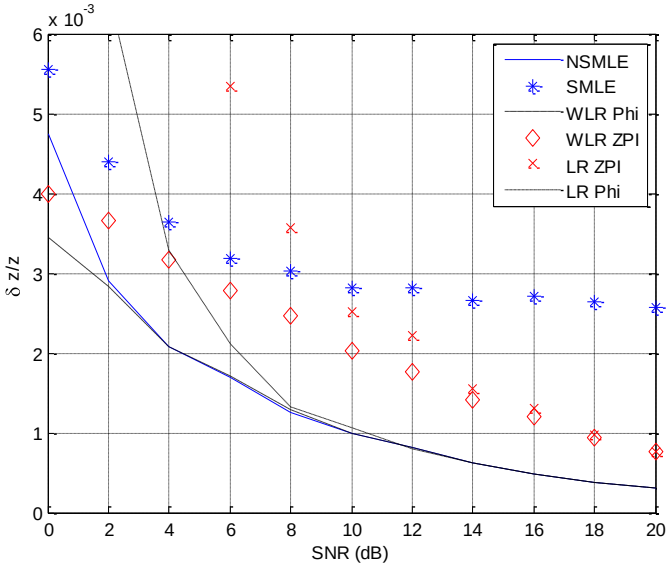

Fig. 3. Relative depth-measurement error obtained by six estimators: nonstationary maximum likelihood estimator (solid line), stationary maximum likelihood estimator ('*' line), phase estimation from linear regression (dashed-dotted line), phase estimation from weighted linear regression (dashed line), zero-phase instant from linear regression ('x' line), and zero-phase instant from weighted linear regression (diamond line). Parameters: H= 23 m, θ_s= 50°.

The error comparison resulting from these six estimators is shown in Fig. 3. First, it appears that the estimation errors are lower for LR Phi and WLR Phi if the phase in the center of the analysis window is used rather than the ZPI. Second, the SMLE obtains poor results for low SNR compared with other estimators such as LR Phi and WLR Phi, due to the unstable characteristics of interferometry. Moreover, Fig. 3 demonstrates the great benefit of using an estimator adapted to the evolution of phase. Indeed, the NSMLE is not applied to the phase $\Delta\varphi$ as done by the linear regression, but to the complex signal S_1S_2*. As a result, the NSMLE is not affected by the presence of phase jumps and delivers promising performances. This could be an asset for large baseline interferometers (generating phase discontinuities) or beam apertures used by sidescan sonars or MBES to process data from outer beams close to 2π. In conclusion, the non-stationary approach represents one solution to noise reduction with phase ambiguities during sounding processing among other techniques based on correlating information between each sensor of an array.

D. What can we expect from interferometric bathymetry: Guide to the Reader

Although interferometric measurement is simple in principle, it can be interesting to compare it to other goniometric techniques which use the same kind of information (correlation), and to examine the result of processing data coming from larger baselines in order to improve performance. Two main drawbacks are involved in the evaluation of the interferometry equation (6). As interferometry processing depends on the quality of the signal, the first drawback is the need to distinguish the phase samples containing bathymetric information from noisy samples. The second is that estimating the phase rotation counter m of each phase sample may be needed according to the interferometer configuration, i.e. large or narrow baselines.

This paper proposes a set of processing enhancements in order to extract greater precision in seafloor depth, capture of in-water objects generally not captured with conventional techniques, and reduction of computational burden in generating images and bathymetric maps. The reading may be difficult for a general readership at first glance, but behind each equation, we have tried to give them a comprehensive meaning by showing the interest of having them.

We have divided this paper into five sections. In the introduction, we have presented the interferometry principle and two solutions for bathymetry purposes: detection of the zero-phase instant, and conversion of each phase sample into an angular

measurement. In order to success in the transition from one simple approach to the other, Section II describes a solution based on a probability model, that is, evaluation of the quality of phase samples and analysis of interferometry performance prediction, making it possible to reject samples without information. This section may be the most cumbersome for a general readership. After introducing our solution, in Section III we compare interferometry processing with other well-known performing techniques in order to quantify if it is worthwhile implementing the interferometry method. It turns out that the proposed modeling provides similar results to other techniques, but with a lower computational burden. This way, we justify the interest of such processing. Then, knowing that interferometry can challenge other techniques, the next step reported in Section IV consists of proposing how to implement optimally interferometry to current MBES. In this section, we integrate the contributions of Sections II and III into a bathymetry algorithm that enables the removal of phase ambiguities and optimizes the performances of interferometers with respect to computational time and spatial resolution. Finally, in Section V we show the experimental bathymetry results of such processing obtained from shipwreck inspections (involving complex in-water targets). From a particular set of experimental data, we quantify the reduction of number of beam formings and the increase of resolution, and we demonstrate the potential of the interferometric information contained in the cross product $S_1S_2^*$.

II. PERFORMANCE EXPECTATION

One of the main difficulties of interferometry, apart from the SNR level or multipath arrivals, concerns the sensitivity of phase measurements to the baseline length. Indeed, the baseline is only a few wave lengths long, while the two-way propagation-path distance is several hundred wave lengths long. As a result, a small error due to noise on the signal can rapidly damage the quality of the DOA estimation. Furthermore, the impact of noise in a phase measurement is not only important in terms of accuracy and performance prediction, but also in terms of confidence on the acquired data to build nautical charts. This section is devoted to the analysis of the correlation coefficient, which plays a central role in the accuracy determination and bathymetric performance estimation (Bird, 2005).

A. Correlation coefficient-based prediction

The statistical behavior of the interferometric signal is at the heart of the problem as it allows the bathymetric mean square error to be derived. The backscattered signal s_i received by the i-th sensor can be modeled as a second-order circular Gaussian process (Sintes, 2010) for high frequency sonar. The main sources of signal degradation found in phase-difference measurements can be divided into two classes: intrinsic noises, corresponding to phenomena responsible for signal decorrelation, and extrinsic noises, such as roll effects or water velocity fluctuations, which directly degrade the bathymetry measurements. Note that both interferometry and beam forming are based on the Huygens principle, and the correlation between signals turns out to be an important indicator of the measurement quality.

Intrinsic noises are a combination of four phenomena: angular decorrelation, spatial decorrelation or sliding footprint, ambient noise, and multipath. The decorrelation phenomena occur when two closely spaced receivers do not see exactly the same resolution cell because of the spacing between them (range-shift decorrelation *aka* sliding footprint) or when the interference patterns of backscattered signals are slightly different, resulting in a loss of coherence between the two receiver outputs (angular decorrelation *aka* baseline decorrelation). The first decorrelation can be minimized by a pre-registration of signals (Sintes, 2010). Multipath propagation is also a cause of fading by interfering with the backscattered signal and damaging the reception of the wave front of the main signal. This phenomenon can be very detrimental for outer beams depending on sidelobe levels. Finally, the ambient noise features several contributions such as surface agitation, living organisms, ship traffic noise, and internal noises of sonar systems, both acoustical and electrical. The more severe phenomena are decorrelation and ambient noise, at the nadir

angles and at the ends of the swath respectively.

The aim now is the fusion of these degrading phenomena into a predictive error model. Traditionally, any phenomenon causing a loss of correlation level is separately studied (Denbigh, 1989; Jin, 1996; Lurton, 2000) and their impacts on the bathymetry are root-mean squared (RMS) accumulated. However, in (Sintes, 2010) the noise aspect was not analyzed as a classical additive perturbation, but as a decorrelation between receivers. Thus, the proposed coherent error fusion (CEF) made it possible to directly integrate the impact of degrading phenomena into the probability density function (PDF) of interferometric phase and thus to improve the accuracy of the bathymetric performance prediction compared with a classical root mean squared error integration. Indeed, the interferometric PDF, widely available in the literature (Tough, 1994; Oliver, 2004) and expressed in (12), only depends on the correlation coefficient ρ:

$$f(\Delta\varphi) = \frac{1-\mu^2}{2\pi}\left[\frac{1}{1-\beta^2} + \frac{\beta}{(1-\beta^2)^{3/2}}\left(\frac{\pi}{2} + \sin^{-1}(\beta)\right)\right] \tag{14}$$

In this equation $\beta = \mu\cos(\Delta\varphi - \phi)$, and μ and ϕ denote the modulus and phase of the correlation coefficient. The interest of the correlation coefficient lies in the information that it delivers: the delay between the two signals coming from the sea. The cross product $S_1S_2^*$ represents a particular form of cross correlation (integration during one time sample) between two sensors. So by computing $S_1S_2^*$ we create an estimator of the time delay. In practice, hydrophones composing an antenna record underwater sound. The signal received before and after the arrival of the wave is considered as noise because it contains no useful information for bathymetry applications. This noise is usually modeled as an uncorrelated circular Gaussian process (Tough, 1994; Jin, 1996). The property of being uncorrelated means that the expected value of the cross product of noises recorded by each receiver is zero. Conversely, the useful signal, corresponding to the backscattered acoustic wave front, is roughly the same on both receivers and therefore, such expectation yields values close to one. Therefore, the computation of the correlation coefficient represents a way to distinguish useful signal from noise. The analytical expression of the correlation coefficient is written in (15) and corresponds to the cross product $S_1S_2^*$ normalized by the energy of both signals.

$$\rho = \frac{E\{s_1 s_2^*\}}{\sqrt{E\{s_1 s_1^*\}\,E\{s_2 s_2^*\}}} = \mu\,\exp(j\phi) \tag{15}$$

S_1 and S_2 stand for the backscattered signals received by the two receivers composing the interferometer, and $E\{x\}$ denotes the mean value of a parameter x. We note in (14) the importance of the correlation coefficient as it controls the shape of the interferometric PDF. For a given phase difference Δφ between signals, the higher the correlation between received signals, the higher the PDF and the better the SNR level, and vice versa. In other words, a good interference between signals, needed for the beam forming process, leads to a high correlation. Therefore, if we are capable of integrating phenomena that cause a loss of signal quality into the evaluation of the correlation coefficient, then the resulting model will give us access to the contribution of each phenomenon to the bathymetric measurement error. As a result, we will be able to distinguish which particular phenomenon is disturbing a bathymetry the most during a survey and then, try to find ways to compensate for it on board. After several derivations we obtained, in (Sintes, 2010), a general expression for ρ that embeds the effects of all phenomena mentioned and that permits coherence estimation:

$$\rho = \mu_D \mathrm{E}_s \exp\left(j\frac{2\pi}{\lambda}B\sin(\theta_s - \theta_0)\right) + \mu_{D,i}\mathrm{E}_i \exp\left(j\frac{2\pi}{\lambda}B\sin(\theta_s - \theta_i)\right) \tag{16}$$

where E_s stands for the backscattered signal energy, E_i is the interference signal energy associated with the multipath contribution,

μ_{Di} contains the spatial and angular decorrelation of the resolution cell projected on the sea surface, and

$$\mu_D = \left(\frac{D_x - |\Delta_x|}{D_x} \right) \mathrm{sinc}\left[\frac{\pi B}{\lambda H} \cos(\theta_s - \theta_0) \cot g(\theta_0) \left(\frac{cT}{2} - B|\sin(\theta_s - \theta_0)| \right) \right] \tag{17}$$

where D_x denotes the footprint length at the grazing angle, Δ_x stands for the footprint shift, and θ_0 is the arrival angle at the position x_0 corresponding to the center of the intersection of the two footprints. All of these parameters are depicted in Fig. 1 and analytically defined in (Sintes, 2010). This series of equations demonstrates that the possible effects of signal and receiver decorrelations can be quickly quantified provided that the sonar equipment is correctly calibrated. Moreover, (17) was obtained for a single frequency wave pulse, but can be adapted to other types of signals, such as chirp signals, in the far field for spatially stationary Gaussian noise.

In conclusion, the correlation coefficient is the keystone of this model and must be estimated either by integrating a prediction of all the involved phenomena, both extrinsic (environment effects) and intrinsic (decorrelation), or through an ad hoc algorithm. The following section presents an attempt at estimation.

B. Correlation coefficient estimation for multisensor systems

Giving the importance of the correlation coefficient ρ to our modeling, the challenge now is to find ways to measure it. Indeed, the correlation model given by (16) required the knowledge of several parameters such as the backscattered signal energy or the interference signal energy that are not always available or not always well defined. One approach to estimate the correlation coefficient is to evaluate the expected value of the conjugate product $S_1S_2^*$ at an instant t_k, based on the neighboring samples:

$$E\{s_1 s_2^*(t_k)\} = \frac{1}{2l+1} \sum_{i=-l}^{l} s_1(t_k + i) s_2^*(t_k + i) \tag{18}$$

The term $s_2(t_k+i)$ represents the signal received by the second sensor at an instant t_k+i, and the term $2l+1$ is the length of the sliding window centered on the sample t_k under consideration. In other words, the correlation coefficient at a given instant t_k is measured from the average of the neighboring time samples (t_k+i). Physically speaking, this may not be accurate enough for low sampling rates, short wavelengths or non-stationary signals as neighboring time samples may not have any relationship between them.

Another solution is to take advantage of the multisensor array geometry of MBES. Based on the Welch estimator, the array is split into multiple pairs of overlapping sub-arrays, each one providing a measurement of signals s_1 and s_2 (see illustrative sketch in Fig. 4). Then, the expected value of the cross product is obtained from these measuerements.

$$E\{s_1 s_2^*(t_k)\} = \frac{1}{p} \sum_{i=1}^{p} s_{1,i}(t_k) s_{2,i}^*(t_k) \tag{19}$$

The term $s_{1,i}(t_k)$ denotes the value of signal s_1 received by the pair i of sub-arrays at sample time t_k, and p denotes the number of pairs of sub-arrays. This time, the correlation coefficient can be instantaneously measured at each sample time, independently of its neighborhood. We do not need to know what happen before and after a given time sample. This solution is already used in other fields to smooth for instance the covariance matrix and thus improve the detection capabilities of subspace-based methods (Krim, 1996). A discussion of the optimal number p of sub-arrays can be found in (Rao, 1990).

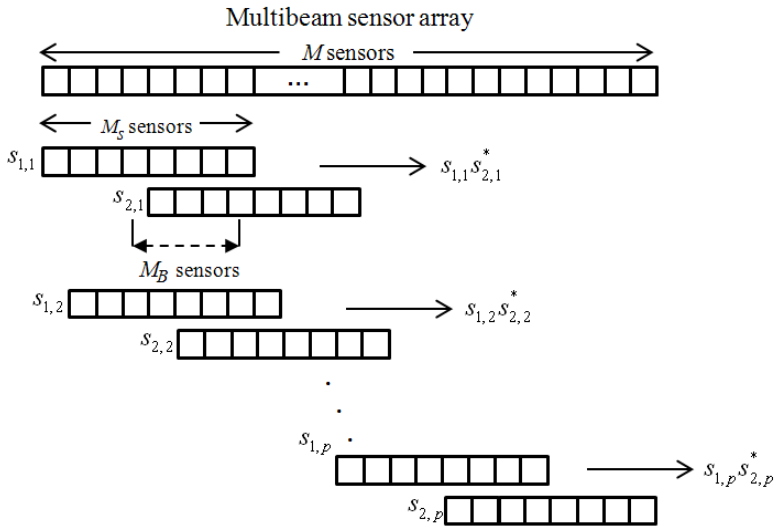

Fig. 4. Sketch showing a way to instantaneously estimate the correlation coefficient based on (19): the multisensor array (top) is split into several pairs of subarrays, each one providing a measurement of the cross product $S_{1,i}S^*_{2,i}$. Then, the correlation coefficient can be determined from the average of measurements as given in (19).

A comparison between these two solutions is shown in Fig. 5. The point-wise approach (18) (upper plot) was obtained from a 9-sample sliding window ($l=4$), whereas signals s_1 and s_2 in (19) (lower plot) were collected with sub-arrays composed of 30 sensors, 15 sensors apart. As the multibeam array was composed of 80 sensors, 36 pairs of sub-arrays (i.e. $p=36$ realizations of the same process) were generated. See in Fig. 5 that both plots have a similar shape, but the sub-arrays-based computation permits a better detection of drops of signals. This result could be expected because the average carried out in (18) acts as a correlation smoothing that filters out drops of signals.

Finally, the form of the correlation coefficient and its relation with the interferometric phase are to be emphasized. Indeed, most of phase samples obtained from a MBES do not provide any useful information. Only those within the acoustic beam can be exploited as shown in the lower panel of Fig. 5 (from samples #600 to #800). Note the low correlation level of noisy samples (middle panel) compared with samples within the acoustic beam. As correlation values are limited between 0 and 1, a way to reject poor samples is to provide thresholds (f.i. 0.80) that permits phase samples to be marked as useful samples if their value is greater than same threshold value, or as noise otherwise (Llort-Pujol, 2012a). This also constitutes a potential step in the denoising direction.

C. Application of the coherence model

A correlation coefficient of 0.7 or 0.8 may be difficult to interpret as high or low. However, there are equations such as (20) that permit this parameter to be converted into a signal-to-noise ratio (SNR) level (Jin, 1996).

$$\mathrm{SNR} = \frac{\mu}{1-\mu} \tag{20}$$

Now, the analysis previously carried out which permitted the identification of the most degrading phenomena can now be expressed in terms of SNR.

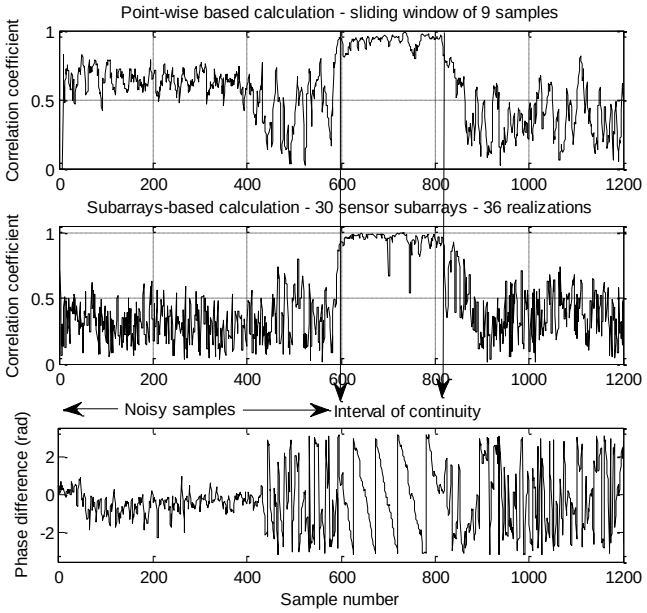

Fig. 5. Estimation of the correlation coefficient (after beam forming at 55°) based on the point-wise approach (18) (upper plot) compared with the estimation based on sliding pairs of sub-arrays, each one providing a realization of signals S_1 and S_2. The result is the generation of an interval of continuity as described in Section IV-A. Parameters: f= 300 kHz, z= 23 m

Another parameter widely used by hydrographers and sonar suppliers is the signal variance that is usually used to compare bathymetries, estimators or measurements. The variance is a measure of the amount of variation of the signal; the lower the variance, the lower the uncertainty of a measurement. Equation (9) shows that the interferometry error is directly proportional to the depth-measurement error. The goal now is to convert a correlation measurement into a variance level. The first step for this goal was to express the correlation in terms of SNR through (20). Then, in (Llort-Pujol, 2011) we derived empirical interferometric variance expressions obtained after analyzing the interferometric signal in both single look and multilook cases. The notion of *multilook* arises when several independent snapshots are collected from the same resolution cell. As the return signal is random due to the contribution of multiple scatterers inside the considered cell, N measurements are averaged to estimate an arrival angle, resulting in a reduction of the signal variance level. In the single look case, i.e. N=1, the interferometric variance can be evaluated using the following simple expression:

$$\mathrm{var}_{SLK}\ \ \Delta\hat{\varphi}\ = \frac{\gamma + \ln(\mathrm{SNR}+1)}{\mathrm{SNR} + \gamma\dfrac{3}{\pi^2}} \tag{21}$$

The term $\mathrm{var}_{SLK}\ \ \Delta\hat{\varphi}$ detones the variance of the interferometric estimator $\Delta\hat{\varphi}$ in the single look case. In the multilook case we have:

$$\mathrm{var}_{MLK}\ \ \Delta\hat{\varphi}\ = \frac{1}{(N-1)\mathrm{SNR} + \dfrac{3}{\gamma_N \pi^2}} + \frac{1}{\dfrac{(N-1)(N-2)}{N}\mathrm{SNR}^2 + \dfrac{3}{(1-\gamma_N)\pi^2}} \tag{22}$$

with N defining the number of independent looks. See that the above expressions only depend on two parameters, SNR and the number of independent realizations N, and both expressions are inversely proportional to these parameters. As a result, the more snapshot we considered (or the higher the SNR level), the lower the variance and the better the accuracy of the estimation..These two simple equations enable a fast and instantaneous evaluation of the depth measurement error. The parameter γ_N is an empirical

fitting term that was derived to improve the agreement between the interferometric variance estimation and the theoretical value. Table I gives different values for γ_N and the corresponding agreement between the theoretical variance value and the estimation as a function of *N*. See that the higher the number *N* of realizations, the better the agreement. This is due to the form of the interferometry variance as a function of the SNR. The computation of the fitting error (third column) was bounded to SNR levels higher than 10 dB because this range of values represents the most common used. For more details, the reader is referred to (Sintes, 2012).

TABLE I
BEST FITTING VALUE OF EMPIRICAL FORMULAS (21) AND (22) AND
ASSOCIATED FITTING QUALITY FOR SNR>10dB

N	γ_N	% of fitting error for SNR>10 dB
1	2.1	1.86
3	5/8	1.24
5	1/2	1.01
11	1/3	1.05
21	1/3	1.21

The difficulty with sidescan sonars, compared with MBES, is that the correlation coefficient is not easily available because we do not have at our disposal an array of sensors to determine the correlation coefficient from (19) as for multribeam echosounders. One solution is to use environmental and propagation models which deliver the different parameters involved in (17) and then estimate the interferometric variance and the correlation coefficient. Indeed, a preliminary coherence estimation can be obtained by measuring the backscattered signal energy, ambient noise energy and interference signal energy, and evaluating (16). Then this coherence estimation is converted into SNR through (20), which in turn is inserted into either (21) or (22) to obtain a phase measurement error. Finally, the depth measurement error is obtained by inserting the latter estimation into (9).

Examples of correlation coefficient estimation, phase variance, and bathymetric accuracy are plotted in Fig. 6, where experimental data was collected with a 455-kHz sidescan sonar. This figure shows three curves corresponding to three ways to compute the correlation, variance and depth error. The first approach (bold gray lines) consists in numerically evaluating the interferometric variance based on its theoretical definition, that is, the integral of the probability density function (14). As this PDF is fully expressed as a function of the correlation coefficient, the theoretical interferometric variance also depends on the correlation. In turn, the correlation coefficient is computed from the prediction model (16) for a given bathymetry scenario (estimation of the backscattered signal and interference energies, footprint length …). The second approach (solid lines) consists in using the empirical variance expressions (21) and (22) which are also fully expressed as a function of the correlation. The third approach (dotted lines) consists in computing the correlation and variance based on experimental data. Thus, Fig. 6 shows that the different curves of these three approaches perfectly overlap. In other words, the simplification of the variance evaluation given by (21) and (22) does not perturb the resulting prediction of the theoretical variance based on a PDF. Nonetheless, the depth errors obtained from numerical (dark line) and empirical (gray line) models for *N=11* and *N=21* do not match the experimental data (dotted line) at all. This is due to the imperfect decorrelation between data samples and the non-stationarity of the interferometric signal. As discussed in Section I.C, the non-stationarity of a signal means that its mean and variance change over time. The more snapshots we use to compute the correlation, the more the mean and variance change with time, and the worst the mismatch between curves. However, the empirical model (gray line) shows perfect agreement with the theoretical

model (dark line). In other words, the simplification of the prediction model (gray line) is in good agreement with the theoretical one.

For bathymetric prediction, developed empirical formulas simplify the complicated processing of second order computation based on interferometric PDF integration (e.g. Fig. 6) and provide formulas accurate enough to be used analytically in performance calculations.

In Fig. 6 the reader can notice the bell-shaped form of the correlation. One could expect a peak of correlation at the beginning of the range with best signal and lower noise. However, experimental data were obtained with a sidescan sonar physically tilted at 60° (=θ_s). As a result the best correlation level is obtained at the interferometric axis. Since the seafloor depth was of 19.4 meters, the peak of correlation is expected around 38.8-meter range as shown in Fig. 6.

In conclusion, due to its simple principle, the correlation coefficient provides a prediction of the bathymetry quality. The equations presented in this section make it possible to validate *in situ* the bathymetric quality and to validate or reject soundings. Moreover, the approximate variance expressions allow a quick manipulation of the variance computation and can also be used for performance prediction of an interferometer based on the coherence model. All these properties make interferometry be a well known and controlled technique. But, one can wonder if the interferometry method can challenge goniometric methods with widely high capabilities of detection with high accuracy such as the Multiple Signal Classification (MUSIC) algorithm or ESPRIT (Estimation of Signal Parameters via Rotational Invariance Techniques). Interferometry PDF and variance are both basically parameterized by the coherence μ (Tough, 1994) that led to the error model discussed in Section II.A. Some goniometric methods are also based on the notion of correlation between sensors. Therefore, the goal of the next section is to investigate whether interferometry can be an alternative method to high-resolution methods when optimally adapted to the receiver system.

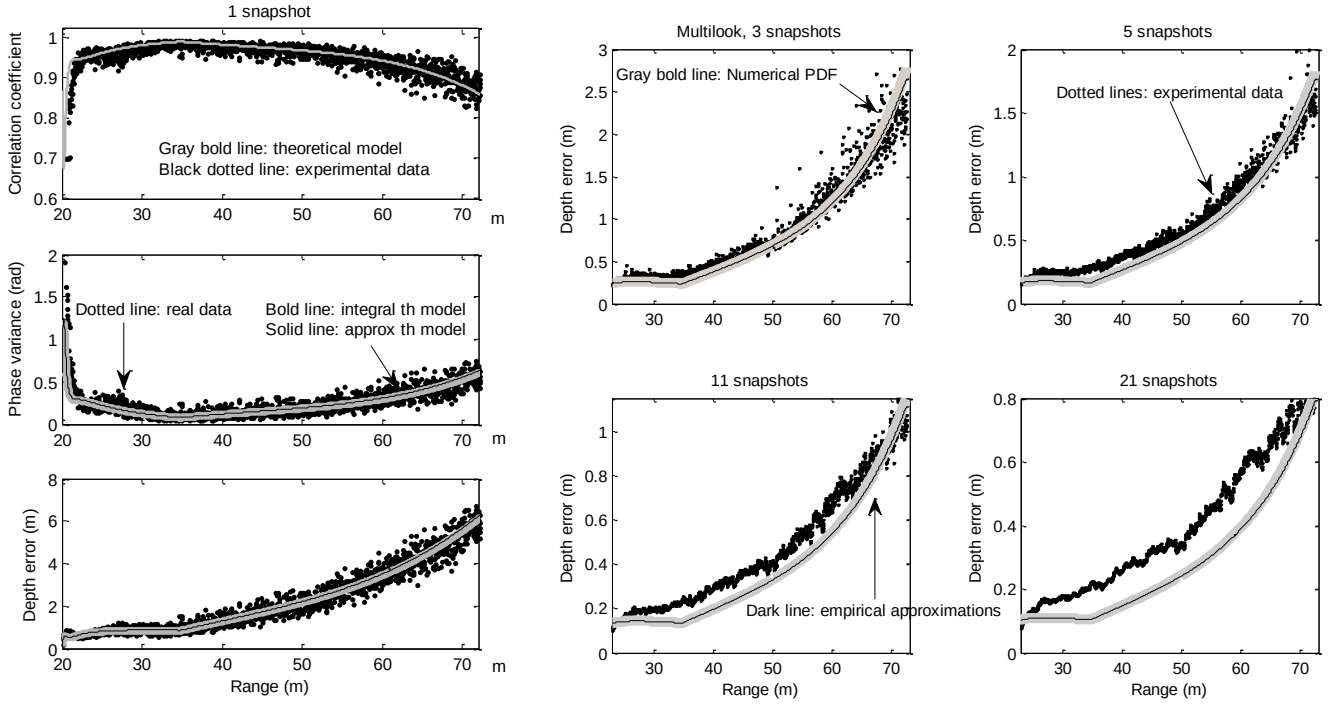

(a) Single-look bathymetric error analysis (b) Multilook bathymetric error analysis

Fig. 6. For the single-look case, the upper figure plots the estimated correlation coefficient based on real data (dark line) and the theoretical model of decorrelation (gray line); the middle figure plots the variance of experimental data (dark line), the phase variance obtained from the theoretical interferometric PDF (bold gray line) and the variance computed through the empirical formulas (21) and (22) (dark thin line); the lower figure plots the same three variances, but expressed in terms of depth-measurement error. The multilook figures plot the same three depth-measurement errors (9) for N=3,5,11,21 snapshots. Interferometric parameters: z= 19.4m, B= 2.5λ, θ_s=60°, and f_c=455 kHz.

III. INTERFEROMETRY AS A CHALLENGER OF GONIOMETRIC METHODS

This section puts interferometry to the test and compares it with high-resolution methods, which are often used in other fields of application (Krim, 1996). Assets and drawbacks of the different techniques are highlighted.

A. Goniometry methods

The complex nature of the backscattered signals makes it possible to detect their arrival using either an amplitude-based or a phase-based approach. A third way consists of locating signal sources through complex signal-based detections, i.e. using both amplitude and phase information. These are the so-called *high-resolution methods* (Krim, 1996), which are mainly based upon the eigen-decomposition of the sample covariance matrix. These methods take advantage of the properties of the signal covariance matrix of the observed sensor outputs to improve the ability to resolve targets. Note that although these techniques were developed for passive detection, they can also be applied to active detection (Ronhovde, 1999).

The high-resolution methods were a breakthrough in array spectral analysis of plane signals received in noise first appearing in the early 1970s. They are particularly appropriate in applications where the observed data consists of harmonic signal components in additive noise of known spectral shape but unknown power level. An especially-important property of eigenstructure-based methods is their ability to provide asymptotic unbiased estimates of the parameters of a multiple signal set, even in the presence of measurement noise. This is an important property because it means that the bathymetry obtained by these methods does not contain a systematic intrinsic error; the method does not contribute to increase possible errors due to noise or decorrelation between receivers.

Many subspace-based methods (Krim, 1996) have been suggested since Pisarenko's pioneering works (Pisarenko, 1973): MUSIC (Bienvenu, 1979) proposed by Bienvenu, Minimum-Norm (Kumaresan, 1983) proposed by Kumaresan and Tuft, ESPRIT (Roy, 1989) proposed by Roy, or CLOSEST vector approach (Buckley, 1990) proposed by Buckley and Xu, among others.

The eigen-decomposition of the covariance matrix allows the estimate of the received signal covariance matrix to be split into orthogonal subspaces named signal and noise subspaces, respectively. The DOA estimation can then be formulated in one of these mutually orthogonal subspaces. For these methods, as well as other spectrum estimation approaches, the DOAs are estimated from the positions of the spectral peaks or, alternatively, from the locations of the nulls of the inverse of the spectrum (called the null-spectrum here). Thus, sources are resolved if the estimated pseudo-spectrum contains maxima at or in the immediate neighborhoods of the true directions of arrival. For instance, the pseudo-spectrum of the MUSIC algorithm that defines the localization function is expressed as:

$$f_{MUSIC}(\theta) = \frac{1}{a(\theta)V_n V_n^* a(\theta)} \tag{23}$$

where $a(\theta)$ stands for a steering vector and V_n are the estimated eigen vectors belonging to the noise subspace (Stoica, 1989). Physically speaking, the possible directions of signal arrival are projected on a noise space. As signal and noise are decorrelated in this space, the direction of signals will result in a null value. Inverted, it gives maximum values.

The implementation of spectral methods based on functions such as (22) consists of generating a vector $a(\theta)$ containing all possible DOAs to be tested. Then this vector is introduced into the algorithm, providing a pseudo-power level attributed to each θ. There are other high-resolution methods that, in contrast to the previous approach, do not provide a power spectrum, but rather DOA values that fulfill a condition. Thus, the DOA estimation does not depend on the tested values introduced into the algorithm; it is the algorithm itself that gives the exact values. The estimated DOAs are obtained from the solution of an analytical equation, e.g. the nearest roots to the unit circle for the polynomial methods (Barabell, 1983) or the highest eigenvalues

for ESPRIT (Roy, 1989).

The main drawback of parametric methods is that they require a specific array configuration (usually uniform linear arrays). Moreover, the estimation of the covariance matrix, the evaluation of eigen values and vectors, and the estimation of the number of sources to be detected, are some of the associated processing required for some of these methods that increase the computational cost. The empirical estimator (the sample covariance matrix) is often of poor quality, requiring additional preprocessing (Van Trees, 2002). In addition to this, the ability to resolve closely spaced sources is dramatically reduced for highly correlated signals. One solution is spatial smoothing of the covariance matrix using forward-backward filtering (Shan, 1985; Rao, 1990) based on the Welch estimator used to estimate the correlation coefficient in Section II.B. Such processing induces a random phase modulation which in turn tends to decorrelate the signals that caused the rank deficiency (Krim, 1996).

In conclusion, the existence of multiple sensors may favor the implementation of high-resolution methods to sonar systems. The more sensors are available, the more uncorrelated sources can be resolved. This is particularly an asset in multipath configurations. Furthermore, the accuracy performance of these methods also increases with the number of sensors (Stoica, 1989). Unfortunately, the associated computational time cost is not negligible compared with the low time cost of interferometry-based algorithms. The question now is whether the statistical performances of interferometry and high-resolution methods are comparable (Hislop, 2011). To this end, the high-resolution methods are represented by the MUSIC algorithm due to its broad use.

B. Statistical comparison

Both interferometry and MUSIC aim at determining the arrival angle of the backscattered signal, but in a different manner using two different estimators: the phase difference between two receivers (interferometry) and the phase of the arrival signal (MUSIC). In the following paragraphs their corresponding variances are rewritten as a function of the DOA in order to compare them directly.

As far as the MUSIC estimator is concerned, let us assume a uniform linear M-sensor array with an inter-sensor spacing Δ of one half wavelength. Then the phase ψ of a given arrival signal can be expressed with respect to the arrival angle θ and the inter-sensor spacing as

$$\psi = \frac{2\pi\Delta}{\lambda}\sin\theta \tag{24}$$

From the above equation, the angular measurement error $\delta\theta$ can be expressed as a function of the phase measurement error $\delta\psi$ as:

$$\delta\theta = \frac{\lambda}{2\pi\Delta\cos\theta}\delta\psi \tag{25}$$

Then, for a single DOA, the variance of the MUSIC DOA estimator can be written as proposed in (Stoica, 1989) using (25):

$$\mathrm{var}_{MUSIC}\ \hat{\theta} = \left(\frac{\lambda}{2\pi\Delta\cos\theta}\right)^2 \mathrm{var}_{MUSIC}\ \hat{\psi} \tag{26}$$

$$= \left(\frac{\lambda}{2\pi\Delta\cos\theta}\right)^2 \frac{6}{NM(M^2-1)\mathrm{SNR}}\left(1+\frac{1}{M\,\mathrm{SNR}}\right) \tag{27}$$

The term $\mathrm{var}_{\mathrm{MUSIC}}\{x\}$ denotes the variance of the MUSIC algorithm to estimate the variable x. Moreover, N in (27) is the number of independent snapshots and M is the number of sensors composing the multibeam array. See that the MUSIC variance decreases with the inter-sensor spacing Δ, the number M of sensors composing the array receiver, and the number of snapshots. In other words, the more the sensors we use to compose the receiver array (or the higher the SNR), the lower the variance to

estimate the DOA.

As far as interferometry is concerned, its statistics are given in Section II-C. In order to simplify (22) to avoid the dependence on the weighting parameter γ_N, the interferometric variance can be written simply as (Llort-Pujol, 2011):

$$\mathrm{var}_{INTF}\ \ \Delta\hat{\varphi}\ = \frac{1}{(N-1)\mathrm{SNR}}\left(1+\frac{N}{(N-2)\mathrm{SNR}}\right) \tag{28}$$

Again, the variance of the interferometric method to estimate the phase shift, i.e. $\mathrm{var}_{INTF}\ \ \Delta\hat{\varphi}$, is inversely proportional to the SNR level and, under some conditions, to the number N of snapshots. In order to compared the interferometric variance with the MUSIC variance, we want to quantify the variance of the interferometric method to estimate the DOA, and thus compared it with (27). To this end, two concerns should be addressed. First, the implementation of beam forming, prior to interferometry, increases the output SNR by a factor of the number of sensors M_s composing the sub-arrays with respect to the SNR of an omnidirectional sensor (Thorner, 1990). Second, when the receiving array is tilted at a given angle θ_s, the effective length decreases by a factor of $cos(\theta_s)$. Therefore, the baseline B can be decomposed as

$$B = M_B \Delta \cos\theta_s \tag{29}$$

where M_B denotes the number of sensors between the centers of the sub-arrays and Δ stands for the spacing between sensors, usually half wavelength. Consequently, the interferometric variance of the DOA estimator from two multisensor arrays can be written using the relation (25) and (28):

$$\mathrm{var}_{INTF}\ \ \hat{\theta}\ = \left(\frac{\lambda}{2\pi B\cos\ \theta_s-\theta}\right)^2 \mathrm{var}_{INTF}\ \ \Delta\hat{\varphi} \tag{30}$$

$$= \left(\frac{\lambda}{2\pi M_B \Delta \cos\theta_s \cos\theta_s - \theta}\right)^2 \frac{1}{(N-1)M_s SNR}\left(1+\frac{N}{(N-2)M_s SNR}\right) \tag{31}$$

The variance of the interferometry method to estimate the DOA is inversely proportional to the number M_s of sensors composing the sub-array receiver, the number M_B of sensors between the center of sub-arrays, the SNR level, and the number N of snapshots. Moreover, beams close to the interferometer axis θ_s leads to lower variance because the term $cos(\theta_s-\theta)$ takes its maximal value equal to 1. Conversely, the further the beam angle θ from the axis, the lower the cosine, and therefore the higher the variance.

In order to compare (27) and (31), note that both the interferometry and the MUSIC (approximate) variances were obtained assuming good bathymetric conditions, i.e. large SNR. Therefore, let us neglect the second term in the second bracket of both expressions, supposing that $1/(N^2\mathrm{SNR}^2)\rightarrow 0$, in order to simplify the variance comparison. Furthermore, it is also assumed that the interferometric detection is carried out near the zero-phase difference, leading to $\theta\approx\theta_s$. Under these assumptions, the ratio between MUSIC variance (27) and interferometry variance (31) becomes

$$\frac{\mathrm{var}_{INTF}\ \ \hat{\theta}}{\mathrm{var}_{MUSIC}\ \ \hat{\theta}} \cong \frac{N}{N-1}\frac{M\ \ M^2-1}{6M_B^2 M_s} \tag{32}$$

See now that the ratio between variances depends on the way the multisensor receiving array is split, i.e. on the number M of sensors composing the receiver array, the number M_s of sensors composing the sub-arrays, and the number M_B of sensors between the center of sub-arrays. In order to better interpret the ratio (32), we can define an array-splitting factor α such that

$$\begin{aligned} M_B &= \alpha M \\ M_s &= (1-\alpha)M \end{aligned} \tag{33}$$

As a result, (32) can be rewritten, after some simplification, as

$$\frac{\mathrm{var}_{INTF}\ \hat{\theta}}{\mathrm{var}_{MUSIC}\ \hat{\theta}} \cong \frac{1}{6\alpha^2(1-\alpha)} \tag{34}$$

Equation (34) is a convex function with a minimum for α=2/3 where the ratio between estimators of 9/8 (=1.125). This means that the variance of the interferometry method is always greater than the variance of the MUSIC algorithm, and at best, the interferometric variance is 1.125 times greater than the MUSIC variance. If we consider the standard deviation, i.e. the square root of the variance, then the interferometry standard deviation is 1.06 times greater than the MUSIC standard deviation. In other words, at best the interferometry method has the same standard deviation as the MUSIC algorithm.

Rigorously speaking, this comparison is not fair because the detection surfaces of the two methods are different. Indeed, the MUSIC detection surface is composed of M sensors, while the two interferometer receivers are composed of M_s(=M/3) sensors. Therefore, a fairer interferometric-antenna geometry would be to have two *M/2*-sensor receivers, M elements apart, in order to work with the same number of sensors as with MUSIC. In this case, the ratio between variances (34) becomes 1/3 (0.6 in terms of standard deviation), meaning that interferometry would outperform MUSIC for a split array.

We see that the physical geometry of the array is crucial to improving the performance of interferometry. A splitting factor equal to 2/3 corresponds to a wide baseline and short sub-arrays. The same result will be obtained in Section III-C when deriving the optimal array configuration in terms of minimal angular error.

In conclusion, we have shown that the interferometry method can also be applied to multibeam systems due to its speed and simplicity. The main difference between interferometry and MUSIC is that interferometry provides ambiguous phase estimates, whereas MUSIC is not subject to this problem because the information provided by sensors is not used in the same way. With an interferometry algorithm dealing with ambiguities, the triangulation capabilities are improved compared with MUSIC, which remains an unbiased method. Nevertheless, as mentioned above, MUSIC has the ability to resolves several DOA at the same instant, which is an important capability. But if interferometry is used with appropriate constraints, these drawbacks can be avoided. Indeed, for MBES, beam forming prior to interferometry enables the rejection of signals reaching the interferometer from unwanted directions. The use of large baselines is not a real obstacle provided that the two sub-arrays retain sufficient aperture. Concerning sidescan sonars, good design of the emitter and receiver beam patterns can block echoes coming from the surface even during close approach by the sonar.

C. Optimal interferometry

The way in which the multibeam array is split to apply interferometry affects the shape of the phase difference because the baseline B changes the phase slope (1). A wide baseline increases the number of phase jumps, leads to narrower sub-arrays, and therefore a wider beam pattern and a larger insonified seafloor region. In this way, the number of soundings to be processed increases, as does the decorrelation (Sintes, 2010). Conversely, a narrow baseline leads to wider sub-arrays, reducing the width of the beam pattern and the insonified seafloor region. Although the decorrelation decreases, the triangulation capacity also decreases because of the closeness of the receivers (Denbigh, 1989).

Two array-splitting configurations are usually taken into account by current bottom detectors: α=1/2 and α=1/3. The first configuration is a trade-off between wide baselines with better triangulation capacity and short baselines with lower depth-

measurement error. The advantage of the second configuration lies in the form of the phase ramp. As discussed in Section I-B, most current interferometry-based bottom detectors estimate the position of a sounding through the ZPI and the implementation of short baselines, such as α=1/3, provides long phase ramps, which simplify the detection of the ZPI through a polynomial fit.

The matter now is to determine whether these two widely-implemented configurations are optimal. In (Llort-Pujol, 2006), we proved that the array splitting factor α that is optimal with respect to minimum angular error can be written as:

$$\alpha_{opt} = \frac{5 + 4v - \sqrt{(+4v)^2 + 8v}}{6} \tag{35}$$

with v depending on the antenna degradation coefficient β, aperture efficiency η, multibeam receiver width l and length L, and input SNR_i:

$$v = \frac{\lambda^2}{8\pi\beta\eta lL\cos(\theta - \theta_s)\,\mathrm{SNR}_i} \tag{36}$$

We also showed in (Llort-Pujol, 2006) that for several MBES, this optimal splitting factor α is bounded between 1/2 and 2/3, and that for SNR_i>-30 dB, α_{opt} is almost constant around 2/3. This range is counter to the sub-array configuration that is usually implemented because the optimal array splitting uses a wide baseline and narrow sub-arrays. To reinforce this result, the relative angular error $\varepsilon(\alpha)$ produced when the optimal baseline is not taken into account was evaluated for several input SNR levels:

$$\varepsilon(\alpha) = \frac{\delta\theta(\alpha)}{\delta\theta(\alpha_{opt})} \times 100 \tag{37}$$

with the angular error $\delta\theta(\alpha)$ and α_{opt}=2/3. The result is plotted in Fig. 7. We see that for SNR=0 dB, this error ratio is about 8.8% greater than the optimal baseline for α=1/2 and about 42% greater for α=1/3. For other SNR_i levels these ratios change, but the convex form of the relative angular error remains the same with an optimal baseline ranging from L/2 for very low SNR_i to 2L/3 for practical conditions.

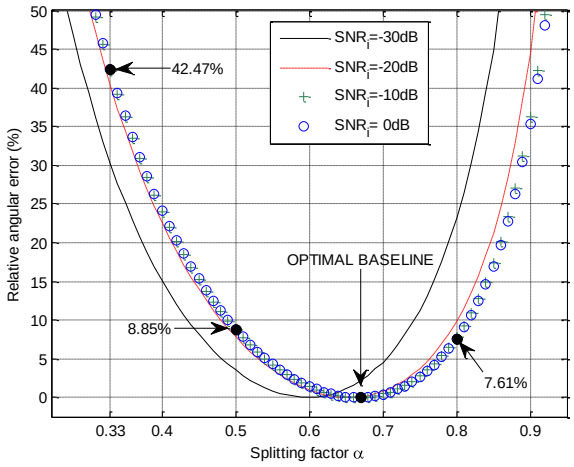

Fig. 7. Evaluation of the relative angular error (37) as a function of the array-splitting factor α (with a baseline composed of αM sensors) relative to the optimal array splitting α_{opt}=2/3. Parameters: input SNR: -30 dB, -20 dB, -10 dB, 0 dB, λ: 5.2mm, array size: 20.15 cm x 5 cm (L x W).

One of the consequences of using narrow baselines is that the DOA accuracy increases, as shown in Fig. 7, and a harder smoothing filter is necessary to compensate for the lower accuracy. In order to obtain similar depth-measurement accuracy levels for the wide and narrow baseline configurations, the complex signal issued from a narrow baseline should be smoothed out with a

longer sliding window to reduce the fluctuation. Consider the following simulation: a flat seafloor with a 50-meter depth was simulated using the parameter settings of a 300-kHz MBES. Five beams were formed at 40°, 45°, 50°, 55°, and 60° with wide- and narrow-baseline interferometers. The standard deviation of the resulting five phase differences was computed and then converted into a relative depth-measurement error based on (9). A comparison of depth-measurement errors is given in Table II (left-hand table), showing that without any phase smoothing, a narrow-baseline interferometer leads to a more fluctuating phase difference. See then that, in order to obtain similar depth-measurement accuracy levels for the two baseline configurations, the complex signal issued from a narrow baseline should be smoothed out with a longer sliding window to reduce the fluctuation. For instance, Table II (right-hand table) shows the depth-measurement error obtained with a sliding smoothing window of 15 points for the narrow-baseline interferometer (α=1/3) and of 5 points for the wide-baseline interferometer (α=2/3). Therefore, using the optimal-baseline configuration not only permits a better angle estimation, but also makes it possible to implement softer noise smoothing (Llort-Pujol, 2012a).

Again, the interferometric estimator (i.e. the argument of S_1S_2*) represents a good trade-off between acceptable statistical performance and simple implementation with multibeam arrays. Thus we increase spatial resolution by taking more soundings per beam into account, while recognizing that the use of wide baselines leads to more phase ambiguities to be handled.

In conclusion at first glance, the interferometry method applied to sonar systems can appear less performing than advanced goniometry techniques as it only uses two receivers. However its detection capability is highly enhanced when applied to multi-sensor arrays together with beam forming. In particular due to the sparse features of the interferometry principle, the increase of the baseline improves triangulation capabilities over classical goniometric techniques, but in return it entails phase ambiguities. As the intrinsic drawbacks of interferometry (2π ambiguity removal, distinction of useful phase samples, or interferometer design) need to be compensated for, the last part of this paper deals with these issues by integrating the coherence error model and optimal array splitting.

TABLE II

EVALUATION OF THE RELATIVE DEPTH-MEASUREMENT ERROR (9) USING TWO BASELINE CONFIGURATIONS AND APPLIED TO RAW (LEFT) AND SMOOTHED (RIGHT) PHASE DIFFERENCE

Without signal smoothing

θ	$\left.\frac{\delta z}{z}\right\|_{\alpha=1/3}$	$\left.\frac{\delta z}{z}\right\|_{\alpha=2/3}$
	N=1	N=1
40°	1.32%	0.63%
45°	1.49%	0.64%
50°	2.36%	0.70%
55°	1.95%	0.68%
60°	3.31%	0.83%

With signal smoothing

θ	$\left.\frac{\delta z}{z}\right\|_{\alpha=1/3}$	$\left.\frac{\delta z}{z}\right\|_{\alpha=2/3}$
	N=15	N=5
40°	0.17%	0.14%
45°	0.14%	0.12%
50°	0.13%	0.13%
55°	0.13%	0.15%
60°	0.16%	0.17%

IV. A FEASIBLE OPTIMAL BATHYMETRY BASED ON AMBIGUOUS INTERFEROMETERS

This last section demonstrates how classical interferometric processing can be improved, resulting in high-resolution bathymetry.

A. Introduction

In order to increase the resolution of bathymetric detections, we propose here an algorithm based on the exploitation of the maximum quantity of information provided by sonar systems, while recognizing that not all phase samples can, or should, be used. The parameter used to distinguish useful samples from noisy ones is the correlation coefficient. It was the fact that the interferometry PDF and the resulting variance only depend on the correlation coefficient that led us to develop an error model based on this parameter. Therefore, the evaluation of the correlation coefficient of each complex sample yields the SNR quality (20). When a seafloor discontinuity occurs, the coherence level drops drastically. Conversely, when the wave front reaches a new object in the scene, the coherence level increases. Therefore, any coherence sample lower than a given threshold (statistically defined) is rejected. In this way the limits of a target within a beam will be defined by the rise and fall of the coherence. An *interval of continuity* (Sintes, 2000; Llort-Pujol, 2006) is thus defined to be the set of samples continuously exceeding a coherence threshold. An example is shown in Fig. 5. Such a set of samples can be ascribed to a common (and unique) target; homogeneity and continuity within the interval of continuity are guaranteed. It now remains to remove 2π phase ambiguity.

B. Phase unwrapping and multisensor design

The implementation of the optimal interferometry configuration discussed in Section III-C leads to an ambiguous interferometric phase. A naive unwrapping algorithm based on the detection of π phase jumps and the increment of the phase rotation counter m may fail to remove the ambiguity of phase ramps when encountering repeated short discontinuities (Lin, 1992). However, the introduction of the notion of an interval of continuity guarantees that all phase samples inside the same interval have the same phase rotation counter.

To take advantage of the spatial diversity, a multi-tool method called Vernier not only makes it possible to remove ambiguities of phase for individual samples (Sintes, 2000; Llort-Pujol, 2008), but can also be used to design interferometers (Sintes, 2011). This double utility makes it interesting for MBES and sidescan sonars. The Vernier method differs from other techniques in requiring at least three aligned sensors to create two pairs of receivers (two interferometers) to determine the phase ambiguity (Denbigh, 1989) (see interferometry geometry in Fig. 1). For each interferometer, we can write the interferometry equation (4) as:

$$\begin{aligned} \Delta\varphi_1 + 2\pi m_1 &= \frac{2\pi}{\lambda} B_1 \sin(\theta_s - \theta) \\ \Delta\varphi_2 + 2\pi m_2 &= \frac{2\pi}{\lambda} B_2 \sin(\theta_s - \theta) \end{aligned} \tag{38}$$

The subscripts 1 and 2 stand for the parameters of the first and second sensor, respectively. Note that the arrival angle θ has no subscript as the wave front is assumed planar when received (far field) and the two interferometers are assumed to be aligned. The received target echo is thus viewed from the same θ by both interferometers. Rewriting the system of equations (38) as a function of the arrival angle then establishes the following equality:

$$\frac{\Delta\varphi_1 \lambda}{2\pi B_1} + m_1 \frac{\lambda}{B_1} = \sin(\theta_s - \theta) = \frac{\Delta\varphi_2 \lambda}{2\pi B_2} + m_2 \frac{\lambda}{B_2} \tag{39}$$

The unknown parameters are θ_s, m_1 and m_2. $\Delta\varphi_i$ (with $i \in \{1,2,3\}$) are the measured phase differences, and λ and B_i are known from the interferometer specifications. The arrival angle θ can be estimated from the pair (m_1, m_2).

In practice, implementation of the Vernier method is limited by the fact that each pair of sensors provides different noisy phase measurements, so the two sides of (39) are not actually equal. Therefore we replace the equality with a minimization of phase measurements, and the pair (m_1, m_2) can be estimated as follows:

$$(\hat{m}_1, \hat{m}_2) = \arg \min_{\substack{k_1 \neq 0 \\ k_2 \neq 0}} \left\{ \left| \left(\frac{\Delta \hat{\varphi}_1 \lambda}{2\pi B_1} + \frac{k_1 \lambda}{B_1} \right) - \left(\frac{\Delta \hat{\varphi}_2 \lambda}{2\pi B_2} + \frac{k_2 \lambda}{B_2} \right) \right| \right\} \tag{40}$$

This equation means that we compute the difference between the two terms in (40) for all possible (integer) values of k_1 and k_2. Then we search for the minimum of the resulting set of differences. Finally, the estimation of m_1 and m_2 is given by the pair (k_1,k_2) that produce the minimum.

A practical example of Vernier ambiguity removal is displayed in Fig. 8 that corresponds to data collected during a shipwreck survey. The phase differences of two interferometers (with B_1=20λ and B_2=13λ) after beam forming are shown with respect to $sin(\theta_s\text{-}\theta)$, i.e. $\frac{\Delta\varphi_i \lambda}{2\pi B_i}$, in solid and dashed-dotted lines respectively. Then, the three curves are vertically shifted by a factor of $\pm\lambda/B_i$, i.e. k_i=±1. While in Fig. 5, the beam only insonified a section of the seafloor, in this figure the beam at 68° not only insonifies the seafloor, but also part of a mooring cable and part of a shipwreck stern. (The existence of such objects is discussed in the following subsection.) As a result, the three in-water targets detected within the same beam produce three intervals of continuity. The minimum distance (40) between shifted curves for the second and third intervals was obtained for (m_1,m_2)=(0,0), while, for the first interval, the minimum occurs for (m_1,m_2)=(1,1). Note that if we had considered a ZPI approach, only one of these three targets would have been detected as this type of approaches only produces one sounding per beam.

One of the main problems of the Vernier method is the compatibility of the required interferometers: Indeed, not all the configurations are possible (Sintes, 2011). The parameter that permits identification of the most compatible baselines and the design of interferometers is the Vernier efficiency (Sintes, 2011) defined as the minimum of the difference given below:

$$eff_{1,2} = \frac{1}{2} \min_{\substack{m_1 \neq 0 \\ m_2 \neq 0}} \left\{ \left| m_1 \frac{\lambda}{B_1} - m_2 \frac{\lambda}{B_2} \right| \right\} \tag{41}$$

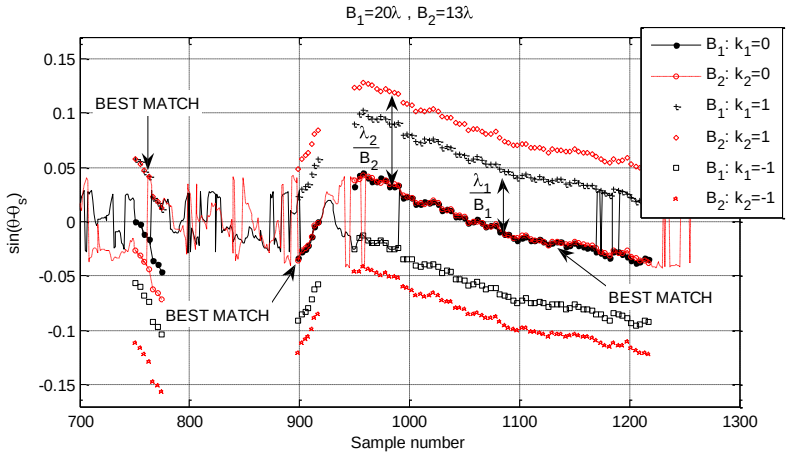

Fig. 8. Example of Vernier ambiguity removal showing the curves created for several values of k_1 and k_2 based on (40). The smallest distance between shifted curves, computed independently for each interval of continuity, defines the correct phase removal. Parameters: B_1= 20λ, B_2=13λ, θ_s=68°, f= 300 kHz, z= 23 m.

Consider the application of the Vernier efficiency to the design of sub-arrays for a multibeam system composed of 80 sensors with half wavelength spacing. As discussed in Section III-C, the optimal way to split sub-arrays is to use a wide configuration with α=2/3. Therefore, the first interferometer is B_1=26.67λ. The following step is to find out the most compatible baseline for the second interferometer need by the Vernier method. Fig. 9 displays the evolution of the efficiency (41) (solid line) with a sawtooth-like form. A minimum of compatibility is obtained when the length of the second baseline equal that of the first interferometer. This result could be expected because if the two interferometers have the same configuration in terms of baselines and sub-array length, then they will produce exactly the same phase difference and no minimization of phase curves will be possible. On the other hand, the maximum compatibility is reached for a second baseline length of 23.82λ.

In practice, not all the values for B_2 can be implemented because the sub-arrays are composed of a finite and integer number of sensors with fixed spacing. Consequently the possible values for B_2, depicted in circles in Fig. 9, correspond to a $\lambda/2$ sub-sampling of the continuous line. In this example, two possible baselines provide similar Vernier efficiencies: either shortening the sub-arrays of the second interferometer by five sensors with respect to the first interferometer (i.e. $B_2=B_1+5\lambda/2=28.68\lambda$), or widening them by four sensors (i.e. $B_2=B_1+4\lambda/2=24.18\lambda$). The second configuration is preferred here because it involves wider sub-arrays receiving more energy.

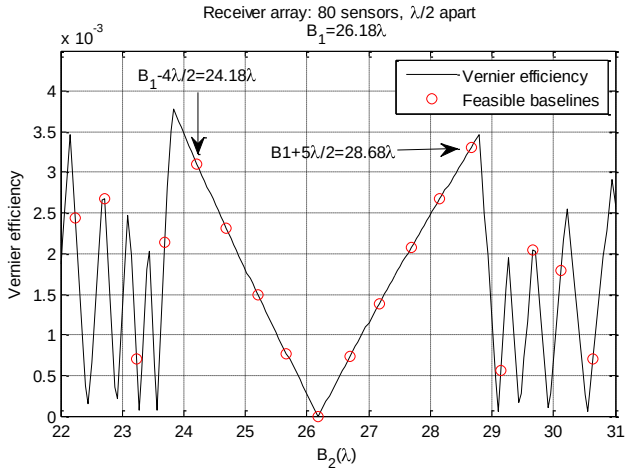

Fig. 9. For a given baseline B_1, the second baseline length can be determined by analyzing the Vernier efficiency (solid line). Applied to multibeam echosounders, only some array configurations are feasible according to the number of sensors composing the sub-arrays (in circles).

In conclusion, we can see the simplicity of designing interferometers with the Vernier efficiency, which makes it possible to benefit from splitting the array to generate larger baselines even though this leads to ambiguities. The same analysis can be carried out for sidescan sonar interferometers but, in this case, it is a matter of hardware design rather than geometry.

C. *Experimental results*

The coherence-based bathymetry algorithm was tested on data collected with a 300-kHz MBES over an area that contained a shipwreck. The multibeam sonar head was mechanically tilted about 40° to the side towards the wreck, which was at a depth of 25 meters. Fig. 10 compares the ship reconstruction obtained by a ZPI-based bottom detector with our coherence-based algorithm (Llort-Pujol, 2012a). Each point in the image corresponds to an estimated pair of coordinates (across-track distance, depth). Moreover, gray colors do not represent any intensity level. The reconstruction was obtained from almost 250 tracks, perpendicular to the shipwreck, each one corresponding to a pulse of sound (or ping). For each track (visible in the upper right panel of Fig. 10), a different number of beams according to the considered bathymetry technique were formed to retrieve the

bathymetry. Thus, the proposed algorithm only formed 18 beams between 25° and 70° to supply about 640 bathymetric soundings, while the ZPI-based detector formed 256 beams to cover the swath. Despite the lower number of beams (18 compared to 256), the proposed algorithm fully exploits the phase difference. Thus, the ZPI principle is "one beam, one sounding" and therefore, the number of soundings composing a bathymetry depends on the number of formed beams. Conversely, our principle is "one beam, several samples", and the final number of soundings per beam depends (somehow) on the sampling rate. For instance, in Fig. 5 the ZPI algorithm would only retrieve one sample, the zero-phase instance, while the proposed algorithm would process about 200 samples. As a result, we do not need to form a lot of beams as one beam may cover up to 5° width of the sea bottom. The improvement is clearly visible in Fig. 10: the four holds and the bow and stern are better described by the coherence-based algorithm. Note particularly the lack of soundings corresponding to the area covering the shipwreck stern in the ZPI image. This is an area of approximately 250 m^2 for which ZPI returned essentially no information while the coherence-based algorithm shows a number of details.

However, the main contribution of the proposed algorithm is the capacity to detect small in-water objects. In this data set a mooring cable was detected over 29 consecutive pings, a continuous detection from the top of the stern to the sea bottom (see lower panel in Fig. 10). Importantly, the coherence-based interferometry processing was 1.59 times faster than the polynomial fitting approach in generating the bathymetry of a ping. This is mainly due to the fact that the coherence-based algorithm formed fewer beams (18 compared to 256) and required a softer filter to reduce the signal fluctuation. Indeed, in order to obtain the same accuracy levels, the complex interferometric signal for the coherence-based interferometry detection was smoothed out with a sliding window shorter than that of the polynomial fitting. Such reduction of the sliding window length lies in the fact that, as shown in Section III-C, the phase-ramp fluctuation level obtained through a wide baseline is almost one third lower than that of a narrow baseline (see Table II). Therefore, the resolution of the continuous detection algorithm was at least three times better than that of the polynomial approach.

A similar algorithm was tested on 450-kHz sidescan sonar data collected over the area where the tanker *Erika* sank off the coast of France in 1999. The results are shown in Fig. 11 where a picture of the *Erika* before sinking and a layout of the ship are compared to the 3-D reconstruction. The interferometry-based algorithm clearly detects and characterizes a number of small in-water objects, including the radar dome, rear masts, and cranes.

The 3-D images show the potential of interferometry-based algorithms for bathymetric detection in complex scenarios such as shipwreck inspections and pipeline tracking. The insonified sea bottom is reconstructed with high resolution, providing small details and detecting in-water targets. This algorithm is just an example of the multiple ways to exploit data coming from a complex array for DOA estimation and shows the high potential of well-designed interferometric sonars.

V. Conclusion: Bathymetry Beyond Interferometry

The interferometry principle makes it possible to reconstruct the subsea bottom with an acceptable statistical performance and a simple implementation to multibeam systems. We have shown that an interferometry-based processing that only searches for the detection of one sample per beam represents a waste of information. Indeed, the $S_1S_2^*$ and the associated phase difference, properly processed, contain a great quantity of information that permits a reconstruction of the scene with a significant increase of resolution and accuracy. An increase in the number of soundings per beam leads to a reduction of beam formings because there is no benefit to forming beams at angles already covered by adjacent beams. Some commercial MBES are already proposing high-density modes for which more than one sounding per beam can be produced, but they do not generally exceed 5 soundings per beam. This quantity represents a low latency if we consider that beams at oblique and grazing angles could provide more than

200 soundings per beam under good detection conditions (obviously depending on the sonar characteristics).

The required processing to select samples containing bathymetric information from noisy one is based on the coherence-based prediction model of Section II and the approximate variance expression of Section III. Furthermore, if the optimal array splitting is considered, i.e. wide baselines and short sub-arrays, the resulting phase difference fluctuates less than with other array configurations and, therefore, it requires softer phase filtering, which improves spatial resolution. This has the added advantage that the computational burden is reduced. Sidescan sonars can also take advantage of *in situ* beam forming to solve some of the difficulties related to phase ambiguity. And processing based on the properties of the correlation coefficient permits sorting out relevant samples to reach the interesting bathymetry. The results plotted in Figs. 11 demonstrate the advantages of such a "risky" approach involving phase ambiguities and large baselines.

Interferometry is clearly an interesting technique that can provide high quality bathymetric data. The approach, with lengthening baselines and an increasing number of ambiguities, can reach its physical limits due to decorrelation. However, spatial decorrelation can be reduced provided that two received signals S_1 and S_2 are co-registered. Even so, baseline decorrelation remains a difficulty. To reach their potential, interferometers must be correctly designed according to the SNR level. This also suggests that largely unexplored approaches such as advanced wide band signals, nonstationary array processing, and synthetic array processing have genuine promise as ways to improve detection accuracy.

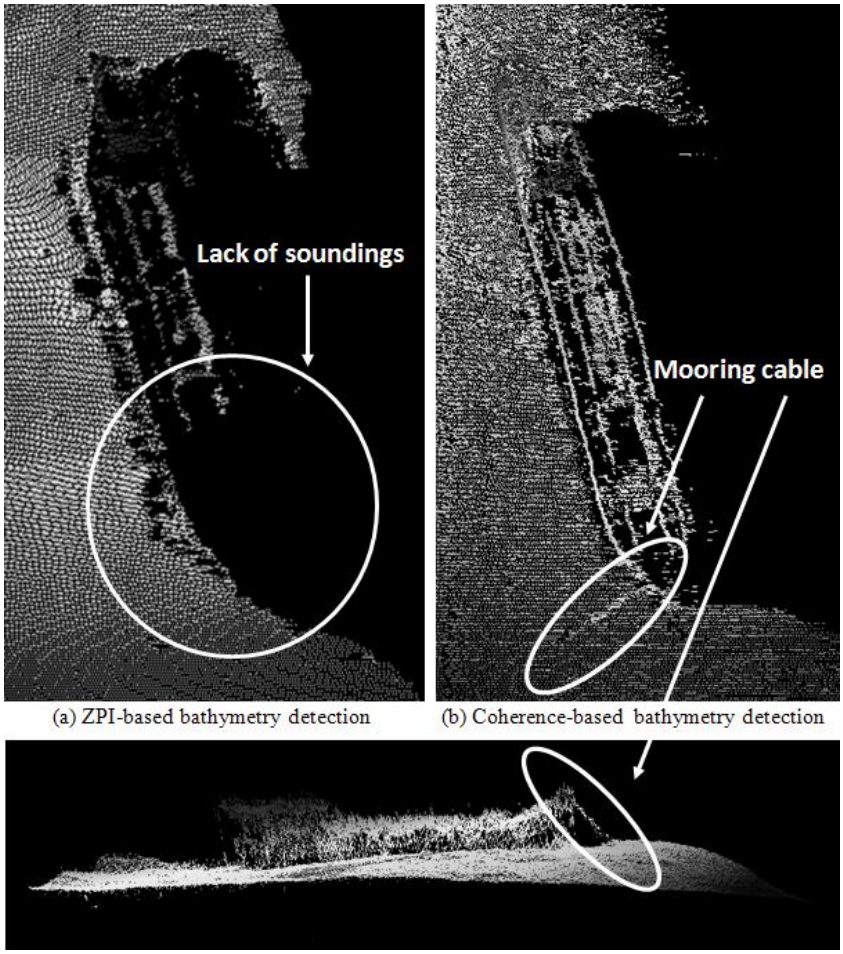

Fig. 10. Three-dimensional mapping of a shipwreck in 25-meter water depth seen from above and showing that the coherence-based bathymetry algorithm (top right and lower panel) is better able to characterize the shipwreck and to detect small, in-water objects such as a mooring cable. The data were collected with a 300-kHz multibeam echosounder.

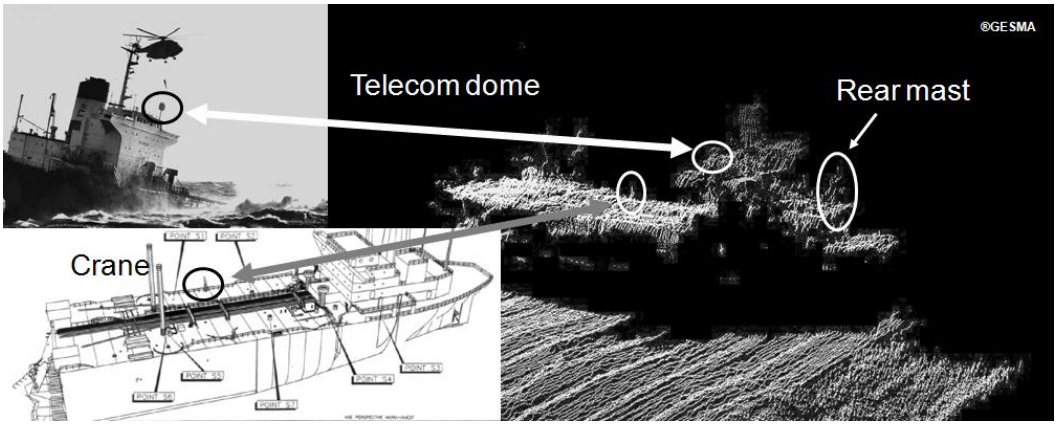

Fig.11. Three-dimensional reconstruction of the tanker *Erika* at a depth of 75m using a 450-kHz interferometric sidescan sonar leading to the detection of in-water targets such as a telecom dome, a rear mast, and a crane. Each pixel in the figure can be converted into a voxel that contains both bathymetry and intensity information (imagery).

ACKNOWLEDGMENT

The authors want to thank DGA/GESMA and Kongsberg Maritime for providing sidescan and multibeam data, respectively. Xavier Lurton is acknowledged for the numerous and interesting discussions about the topics dealt with in this paper. Patricia E. Stiede is also acknowledged for his great help in reviewing the manuscript.

REFERENCES

Barabell, A. J. 1983. Improving the resolution performance of eigenstructure-based direction-finding algorithms. IEEE Trans. Acoust., Speech, Signal Processing. 8: 336–339.

Bienvenu, G. 1979. Influence of the spatial coherence of the background noise on high resolution passive methods. IEEE Trans. Acoust., Speech, Signal Processing. 4: 306–309.

Bird, J. S., and G. K. Mullins. 2005. Analysis of swath bathymetry sonar accuracy. IEEE J. Oceanic Eng. 30(2): 372-390.

Buckley, K. M., and X. L. Xu. 1990. Spatial-spectral estimation in a location sector. IEEE Trans. Acoust., Speech, Signal Processing. 38(11): 1842–1852.

Denbigh, P. N. 1989. Swath bathymetry: Principles of operation and an analysis of errors. IEEE J. Oceanic Eng. 14(4): 289–298.

Kendall, M. G., and A. Stuart. 1961. The advanced theory of statistics. New York: Hafner

Kraeutner, P. H., and J. Bird. 1999. Beyond interferometry, resolving multiple angles-of-arrival in swath bathymetric imaging. In: Oceans'99 MTS/IEEE Conf. Proc. pp. 37–45.

Krim, H., and M. Viberg. 1996. Two decades of array signal processing research: the parametric approach. IEEE Signal Processing Magazine. 13(4): 67–94.

Kumaresan, R., and D. W.Tufts. 1983. Estimating the angles of arrival of multiple plane waves. IEEE Trans. Aerosp. Electron. Syst. 19(1): 134–139.

Hislop., G., and C. Craeye. 2011. On the mathematical link between the MUSIC algorithm and interferometric imaging. IEEE Trans. Antennas and Propagat. 59(4): 1412–1414.

Jin, G., and D. Tang. 1996. Uncertainties of differential phase estimation associated with interferometric sonars. IEEE J. Oceanic Eng. 21(1). pp. 53 – 63.

Masnadi-Shirazi, M. A., C. de Moustier, P. Cervenka, and S. H. Zisk. 1992. Differential phase estimation with the SeaMARCII bathymetric sidescan sonar system. IEEE J. Oceanic Eng. 17(3). pp. 239 – 251.

Llort-Pujol, G., C. Sintes, and X. Lurton. 2006. A new approach for fast and high-resolution interferometric bathymetry. In: Oceans 2006 MTS/IEEE Conf. Proc. pp. 1–7.

Llort-Pujol, G., C. Sintes, and D. Guériot. 2008. Analysis of Vernier interferometers for sonar bathymetry. In: Oceans 2008 MTS/IEEE Conf. Proc. pp. 1–5.

Llort-Pujol, G., and C. Sintes. 2011. Interferometric angle estimation for bathymetry performance analysis. In: Oceans 2011 MTS/IEEE Conf. Proc.

Llort-Pujol, G., C. Sintes, and X. Lurton. 2012a, Multiple-target interferometry detection processing for multibeam high-density soundings. Submitted for publication.

Llort-Pujol, G., C. Sintes, T. Chonavel, Y.Ladroit, A. Sacuan, and X. Lurton. 2012b. Interferometry phase estimator based on non-stationary approach. In: Oceans 2012 MTS/IEEE Conf. Proc. Submitted for publication.

Lin, Q., J. F. Vesecky, and H. A. Zebker. 1992. New approches in interferometric SAR data processing. IEEE Trans. Geosci. Remote Sensing. 30(3): 560–567

Lurton, X. 2000. Swath bathymetry using phase difference: theoretical analysis of acoustical measurement precision. IEEE J. Oceanic Eng. 25(3). pp. 351–363.

Lurton, X. 2003. Theoretical modelling of acoustical measurement accuracy for swath bathymetric sonars. International Hydrographic Review. 4(2). pp. 17–30.

Oliver, C., and S. Quegan. 2004. Understanding synthetic aperture radar images. Boston: Artech House. 479 pp.

Pisarenko, V. F. 1973. The retrieval of harmonics from a covariance function. Geophys. J. Roy. Astronom. Soc. 33(3): 347–366.

Rao, B. D., and K. V. S. Hari. 1990. Effect of spatial smoothing on the performance of MUSIC and the minimum-norm method. IEE Radar and Signal Proc. 137(6): 449–458.
Ronhovde, A., L. Yang, T. Taxt, and S. Holm. 1999. High-resolution beamforming for multibeam echo sounders using raw EM3000 data. In: Oceans'99 MTS/IEEE Conf. Proc. pp. 923 – 930.
Roy, R., and T. Kailath. 1989. ESPRIT - estimation of signal parameters via rotational invariance techniques. IEEE Trans. Acoust., Speech, Signal Processing, 37(7): 984− 995.
Shan, T., M. Wax, and T. Kailath. 1985. On spatial smoothing for direction-of-arrival estimation of coherent signals. IEEE Trans. Acoust., Speech, Signal Processing. 33(4): 806–811.
Shensa, M. and C. Black. 1978. Passive bearing estimation: The removal of bias and 2π ambiguities. J. Acoust. Soc. Amer. 63(1): 91–100.
Sintes, C. and B. Solaiman. 1999. Side scan sonar and interferometric noise. In: Oceans 1999 MTS/IEEE Conf. Proc. pp. 1591–1596.
Sintes, C. and B. Solaiman. 2000. Strategies for unwrapping multisensors interferometric side scan sonar phase. In: Oceans 2000 MTS/IEEE Conf. Proc. pp. 2059–2065.
Sintes, C., G. Llort-Pujol, and D. Guériot. 2010. Coherent probabilistic error model for interferometric sidescan sonars. IEEE J. Oceanic Eng. 35(2): 412–423.
Sintes, C., G. Llort-Pujol, and J. M. LeCaillec. 2011. Vernier interferometer performance analysis. In: Oceans 2011 MTS/IEEE Conf. Proc.
Sintes, C., and G. Llort-Pujol. 2012. Empirical interferometric phase variance formulas for bathymetric applications. IEEE Trans. Geosci. Remote Sens. To be published
Stoica, P., and A. Nehorai. 1989. MUSIC, maximum likelihood and Cramer Rao bound. IEEE Trans. Acoust., Speech, Signal Processing. 37(5): 720–741.
Tough, R. J. A., D. Blacknell, and S. Quegan. 1994. A statistical description of polarimetric and interferometric synthetic aperture radar data. In: Proc. Royal Society. pp. 567–589.
Thorner, J. E. 1990. Approaches to sonar beamforming. In: Southern Tier Technical Conference. Proceedings of the 1990 IEEE. pp. 69–78.
Tribolet, J. M. 1977. A new phase unwrapping algorithm. IEEE Trans. Acoust., Speech, Signal Processing. 25(2): 170–177.
Van Trees, H. L. 2002. Optimum Array Processing: Part IV of Detection, Estimation, and Modulation Theory. New York: Wiley-Interscience.
Yang, L., T. Taxt, and F. Albregtsen. 1997. Bottom detection for multibeam sonars with active contours. In: Oceans'97 MTS/IEEE Conf. Proc. pp. 943–950.